Development of a Theoretical Model of Nickel(II) Tris(oxime)amine Dichloride with Comparison to X-ray Crystallography and Vibrational Spectroscopy

Rebecca M. Jones and Michael J. Baldwin*

University of Cincinnati, Department of Chemistry, P.O. Box 210172, Cincinnati, Ohio 45221-0172

Received: October 16, 2003; In Final Form: January 28, 2004

Using modern density-functional theory and vibrational spectroscopy, various theoretical models are evaluated for application to Ni(TRISOXH$_3$)Cl$_2$, the precursor to a novel oxygen-activating complex. Geometry optimizations and frequency calculations were performed using Gaussian 98 at the Hartree−Fock and B3LYP theory levels. Theoretical data are compared to the published X-ray crystal structure and to vibrational spectra obtained using Raman and infrared methods. The geometry closest to the crystal structure resulted from B3LYP/6-31G(d) & 6-311++G(d,p), where the higher basis set was applied to the metal center. This gas-phase model has a 1.0% average deviation from the experimental bond distances in the solid-phase structure. A lower level calculation (B3LYP/6-31G(d) & 6-311+G(d), again with the higher basis set applied to the Ni) yields vibrational frequencies that are as accurate as the higher level calculation. Three isotope-substituted TRISOXH$_3$ ligands were synthesized (with ^{15}N amine, ^{15}N oximes, or deuterated oximes); the isotope shifts observed in the vibrational spectra of the Ni complexes were compared to the theoretical shifts. With this empirical information, 28 key normal modes of the vibrational spectra were assigned. A modified wavenumber−linear scaling procedure was applied to the assigned theoretical wavenumbers and yielded a 3-fold improvement in absolute deviation from experimental frequencies over the unscaled values.

Introduction

The advent of fast, inexpensive cluster computers and accurate computational chemistry software, used in combination with experimental methods, now provides a powerful approach for chemists tackling difficult questions,[1] especially in the area of transition metal systems.[2,3] However, the development of an appropriate and well-calibrated theoretical model is paramount to the successful application of computational methods. In this work, a theoretical model of a chemically interesting nickel(II) compound is developed and compared to experimental data via X-ray crystallography and vibrational spectroscopy. Given the nature of the molecule of interest, a large transition metal complex with two unpaired electrons, density-functional theory (DFT) is employed as the principle theoretical method. This approach has been successfully employed for studying electronic structure of transition metal systems.[4−8] Various theoretical models were evaluated for accuracy, with regard to prediction of molecular structure and vibrational modes, in order to address the important considerations of theory level and basis set choice.

Our group has developed unique, oxygen-active nickel(II) complexes with tripodal amine ligands incorporating oxime functional groups; upon deprotonation of the oximes, catalytic aerobic oxidation of substrates such as methanol is observed.[9,10] Progress toward this kind of green chemistry, by the development of mass-efficient oxidants and reusable metal catalysts, is of great interest in the 21st century.[11,12] Nickel complexes that activate molecular oxygen are rare, due primarily to the relatively inaccessible higher oxidation states of nickel. However, oximates have been shown to lower the oxidation potential of nickel(II) and stabilize high-valent nickel complexes.[13−17]

* Author to whom correspondence should be addressed. E-mail: Michael.Baldwin@uc.edu.

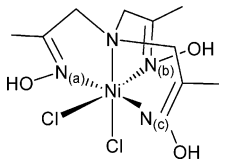

Figure 1. Structure and assigned letter designation for oximes of **1**: Ni(TRISOXH$_3$)Cl$_2$.

A theoretical model may bring tremendous insight into the electronic structure of this candidate oxygen activation catalyst and may be applied to experimentally inaccessible putative intermediates.

The complex chosen for the development of a computational model is Ni(II)(TRISOXH$_3$)Cl$_2$ (**1**, shown in Figure 1.); the tetradentate TRISOXH$_3$ ligand is a tripodal amine with three oxime arms that are coordinated to the metal through the amine and oxime nitrogens. Two chloride ions provide charge balance to the divalent nickel, resulting in a six-coordinate metal center. The crystal structure shows interesting intramolecular hydrogen bonding and a slightly distorted octahedral configuration about the metal site.[10] These characteristics are also observed in the computational model. In this work, various ab initio and density-functional theoretical models are evaluated by comparison of optimized molecular geometry to the X-ray crystal structure. Selected computational models are also assessed by comparison of calculated vibrational modes with experimental Raman and infrared spectroscopy. The theoretical frequencies exhibit less accurate correlation with experimental vibrational spectra than with the crystallographic structural parameters. However, isotopic labeling of the complexes and calculated isotope shifts have facilitated assignment of many important molecular vibrations; this assignment demonstrates a linear correlation between the theoretical and experimental frequencies.

10.1021/jp037139r CCC: $27.50
Published on Web 03/24/2004

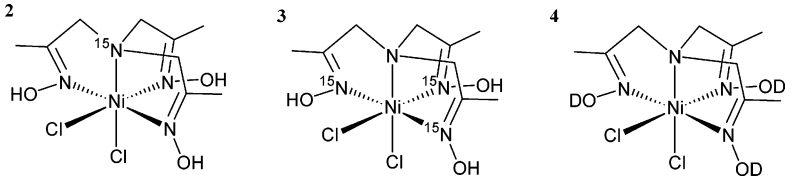

Figure 2. Structure of isotope-labeled complexes. **2**: Ni(TRISOX(^{15}N amine)H_3)Cl_2. **3**: Ni(TRISOX(^{15}N oximes)H_3)Cl_2. **4**: Ni(TRISOXD_3)Cl_2.

Experimental Methods

Isotope-Substituted Complexes. To facilitate vibrational mode assignment, three isotopic substitutions on the organic ligand of Ni(TRISOXH_3)Cl_2 were introduced; these complexes (**2**, **3**, and **4**) are shown in Figure 2. With minor modifications to the published synthesis,[18,19] the amine nitrogen of TRISOXH_3 was isotopically substituted using $^{15}NH_4OH$ (3.3 N in H_2O, 98% ^{15}N, Cambridge Isotope Laboratories, Inc.) to yield the ligand for **2**. In the synthesis of the ligand for **3**, the oxime nitrogens were labeled using $H_2{}^{15}NOH$*HCl (minimum 98+% ^{15}N, Isotec). The Ni complexes of the ^{15}N-labeled ligands (**2** and **3**) were synthesized by previously published methods and recrystallized by vapor diffusion of ethyl acetate into a methanol solution. In the synthesis of Ni(TRISOXD_3)Cl_2 (**4**), substitution of the oxime protons with deuterons was done by dissolving the natural abundance complex in NMR-grade deuterated methanol (99.8% D, Acros) and recrystallizing the complex by vapor diffusion of ethyl acetate.

Vibrational Spectroscopy. Raman spectra were collected using a SPEX 1404 0.85 m double spectrometer with a liquid N_2 cooled 13.6 mm back-thinned SPEX Spectrum-1 CCD chip detector. Raman scattering was excited by the 488.0 or 514.5 nm line of a Coherent 10 W Sabre Ar ion laser; the laser lines were chosen for intensity and the availability of holographic notch filters. The power used was typically 300 mW at the sample, and no sample decomposition is observed. The scattered light was directed through a Kaiser Optical Systems holographic SuperNotch filter for each wavelength. Raman shifts were calibrated against the appropriate Raleigh line. Samples for Raman experiments were prepared by finely grinding the recrystallized complex with an agate mortar and pestle and filling a 1 mm i.d. melting point capillary tube. Samples were cooled to approximately −150 °C by a liquid nitrogen chilled stream of N_2 gas blown through a quartz EPR-type cooling tube (Bruker Instruments). Resulting spectra were 4-point baseline corrected using GRAMS/32 (v5.22), and then multiple spectra were averaged to improve the signal-to-noise ratios.

Infrared spectra were collected using a BioRad Excalibur spectrometer with a DTGS electrically cooled detector; a KBr extended range beam splitter was used for the mid-IR and a Mylar 6.25 μm beam splitter for the far-IR. Samples for mid-IR measurements were dispersed in a KBr pellet. Samples for far-IR measurements were loaded onto 3M Disposable IR Cards (Type 61-100-12, Polyethylene) by evaporation from methanol (D-methanol was used for **4**).

Theoretical Calculations

All theoretical calculations were performed with Gaussian 98, version A.11[20] (G98) on a cluster of 16 Linux nodes, each with a 1.4 GHz processor. Modeling was performed on the entire Ni(TRISOXH_3)Cl_2 molecule; gas-phase geometry optimizations and frequency calculations had neither symmetry constraints nor bond restrictions imposed. Spin-unrestricted calculations on Ni(TRISOXH_3)Cl_2 were first performed at Hartree−Fock levels with the 6-31G basis set; all further calculations used this UHF/6-31G optimized geometry as a starting point. Density-functional calculations principally facilitated the Becke three-parameter hybrid exchange functional[21] and the Lee, Yang, and Parr correlation functional,[22] hereafter abbreviated B3LYP. For comparison, the functional B3P86 was employed, which includes the gradient corrections of Perdew, along with his 1981 local correlation functional.[23] In the development of the theoretical model, the basis set was varied. Often, split basis sets were employed, via the *gen* keyword of G98, applying a higher basis set such as 6-311+G(d) to the metal center and the smaller 6-31G(d) to all other atoms. Generally, all-electron basis sets were chosen for accuracy; however, the LANL2DZ basis set was once applied only to the metal center. A summary of the relevant theory and basis set details is shown in Table 1. Isotope-shifted vibrational frequencies were calculated for the **C** level via the *readiso* keyword in G98.

TABLE 1: Computational Details

	theory level	basis set C,N,O,H	basis set Cl	basis set Ni
A	uhf	6-31G	6-31G	6-31G
B	ub3lyp	6-31G(d)	6-31G(d)	lanl2dz
C	ub3lyp	6-31G(d)	6-31G(d)	6-311+G(d)
D	ub3lyp	6-31G(d)	6-311++G(d,p)	6-311++G(d,p)
E	ub3lyp	6-31G(d)	6-31G(d)	6-31G(d)
F	ub3lyp	6-31G(d)	6-31G(d)	6-311G
G	ub3p86	6-31G(d)	6-31G(d)	6-311G(d)

Results and Analysis

Comparison of the bond distances and angles from the structure of **1**, determined by X-ray crystallography, to the theoretical molecular geometries of models **A**−**D** is presented in Table 2. A visual comparison of the X-ray crystal structure[10] and the optimized geometry of model **D** is shown in Figure 3; notable features that are reproduced in both are a pseudo-octahedral geometry nickel center and intramolecular hydrogen bonding between the oxime protons and axial chloride. On account of the crystal packing forces and intermolecular interactions, perfect correlation is not expected between the geometries generated from the gas-phase calculation and X-ray crystal structure. Excluding those bond lengths that are significantly influenced by intermolecular hydrogen bonding (Ni−N(c) and N(c)−O), the average percent deviation of theoretical from experimental bond lengths is used to quantify the accuracy of the calculations. The baseline Hartree−Fock calculation **A** has the largest deviation from the experimental data, averaging 0.054 Å or 2.6% deviation, resulting in part from the lack of electron correlation. Models **B** and **C** show smaller deviations from experiment, averaging 1.6% and 1.2%, respectively; however, calculation **D** has the smallest percent deviation, 1.0%. In comparison, the average uncertainty for the X-ray crystal structure is 0.0014 Å or 0.095%. Because of their relatively large deviation from experiment, models **E**−**G** (summarized in Table 1S of the Supporting Information) will not be addressed in detail.

One significant feature of the solid-phase structure is reproducible in the gas-phase models; the oxime protons from oxime-(a) and (b) (or O1 and O3 in the ORTEP of Figure 3) exhibit intramolecular hydrogen bonding to the axial chloride. In all

TABLE 2: Geometry Comparison: Ni(TRISOXH$_3$)Cl$_2$ Crystal Structure to Theoretical Models A−D

feature[a]	crystal structure data[b]	**A**[c] uhf/6-31G	**B**[c] ub3lyp/6-31G(d) & LANL2DZ	**C**[c] ub3lyp/6-31G(d) & 6-311+G(d)	**D**[c] ub3lyp/6-31G(d) & 6-311++G(d,p)
symmetry	N/A	C_1	C_1	C_s	C_s
Ni−N1[d]	2.1131(13)	2.2594(0.1463)[e]	2.1963(0.0832)	2.1496(0.0365)	2.1471(0.0340)
Ni−N(a)	2.0367(14)	2.1221(0.0854)	2.0621(0.0254)	2.0304(0.0063)	2.0359(0.0008)
Ni−N(b)	2.0485(14)	2.1936(0.1451)	2.1568(0.1083)	2.1054(0.0569)	2.1004(0.0519)
Ni−N(c)	*2.0957(14)*[f]	*2.1221(0.0264)*	*2.0620(0.0337)*	*2.0304(0.0653)*	*2.0359(0.0598)*
Ni−Cl(axial)	2.4003(4)	2.4637(0.0634)	2.4107(0.0104)	2.4146(0.0143)	2.4249(0.0246)
Ni−Cl(eq)	2.4344(4)	2.4991(0.0647)	2.4000(0.0344)	2.3917(0.0427)	2.4138(0.0206)
C═N(a)	1.274(2)	1.2707(0.0033)	1.2803(0.0063)	1.2812(0.0072)	1.2817(0.0077)
C═N(b)	1.273(2)	1.2672(0.0058)	1.2769(0.0039)	1.2812(0.0082)	1.2789(0.0059)
C═N(c)	1.280(2)	1.2707(0.0093)	1.2803(0.0003)	1.2786(0.0014)	1.2817(0.0017)
N(a)−O	1.3921(18)	1.3881(0.0040)	1.3734(0.0187)	1.3745(0.0176)	1.375(0.0171)
N(b)−O	1.3952(17)	1.3871(0.0081)	1.3688(0.0264)	1.3699(0.0253)	1.3705(0.0247)
N(c)−O	1.4022(17)	1.3881(0.0141)	1.3734(0.0288)	1.3745(0.0277)	1.375(0.0272)
H(a)···Cl(axial)[g]	2.502	2.9477(0.4457)	2.6877(0.1857)	2.6161(0.1141)	2.6621(0.1601)
H(b)···Cl(axial)	2.353	2.3139(0.0391)	2.1336(0.2194)	2.1268(0.2262)	2.1485(0.2045)
H(c)···Cl(axial)	*3.601*	*2.9468(0.6542)*	*2.6855(0.9155)*	*2.6161(0.9849)*	*2.6621(0.9389)*
∠O−N(a)−Ni	125.99(11)	126.13(0.14)	125.22(0.77)	125.49(0.50)	126.07(0.08)
∠O−N(b)−Ni	125.08(10)	125.81(0.73)	124.39(0.69)	125.38(0.30)	125.905(0.83)
∠O−N(c)−Ni	*129.26(10)*	*126.13(3.13)*	*125.20(4.06)*	*125.49(3.77)*	*126.07(3.19)*
∠N(a)−Ni−N1	79.65(5)	77.18(2.47)	125.22(0.77)	125.44(0.55)	80.67(1.02)
∠N(b)−Ni−N1	80.54(5)	76.33(4.21)	124.39(0.69)	125.58(0.50)	79.64(0.90)
∠N(c)−Ni−N1	*77.90(5)*	*77.18(0.72)*	*125.20(4.06)*	*125.44(3.82)*	*80.67(2.77)*
∠Cl(eq)−Ni−N1	94.27(4)	90.52(3.75)	79.3(0.35)	81.44(1.79)	92.93(1.34)
∠Cl(ax)−Ni−Cl(eq)	*96.620(15)*	*107.16(10.54)*	*77.76(2.78)*	*80.11(0.43)*	*101.32(4.70)*
∠N(a)−Ni−Cl(ax)	*92.27(4)*	*102.28(10.01)*	*79.33(1.43)*	*81.44(3.54)*	*99.45(7.18)*
∠N(b)−Ni−Cl(ax)	*88.40(4)*	*85.99(2.41)*	*92.62(1.65)*	*92.14(2.13)*	*86.11(2.29)*
∠N(c)−Ni−Cl(ax)	*110.68(4)*	*102.26(8.42)*	*103.79(7.17)*	*101.89(1.96)*	*99.45(11.23)*
∠Cl(eq)−Ni−N(a)	90.08(4)	89.91(0.17)	100.54(8.27)	98.58(6.41)	88.86(1.22)
∠N(a)−Ni−N(b)	88.18(6)	87.20(0.98)	85.83(2.57)	85.86(10.18)	89.92(1.74)
∠N(b)−Ni−N(c)	*92.80(6)*	*87.20(5.6)*	*100.5(10.18)*	*98.58(12.1)*	*89.92(2.88)*
∠N(c)−Ni−Cl(eq)	*86.88(4)*	*89.90(3.02)*	*89.52(0.56)*	*89.21(0.87)*	*88.86(1.98)*

[a] All bond distances shown in Angstroms, bond angles (∠) in degrees. [b] See ref 10. [c] Theoretical models **A**−**D** are listed with theory level and basis sets; see Table 1 for basis set assignment. [d] Letter designations on atoms have the following meaning: N1 represents the amine, N(a) and N(c) are oxime bound N's trans to each other—equivalent in calculations with C_s symmetry, N(b) is the oxime bound N trans to the equatorial Cl$^-$ (denoted Cl(eq)), Cl(axial) is trans to the amine. H(a) is the proton on the oxygen of oxime with N(a) and similarly for H(b) and H(c). [e] Absolute deviations of calculated values from experimental data are given in parentheses. [f] Italicized experimental values and theoretical deviations indicate those which are perturbed by intermolecular hydrogen bonding. [g] ··· indicates hydrogen bonding and/or through space distances.

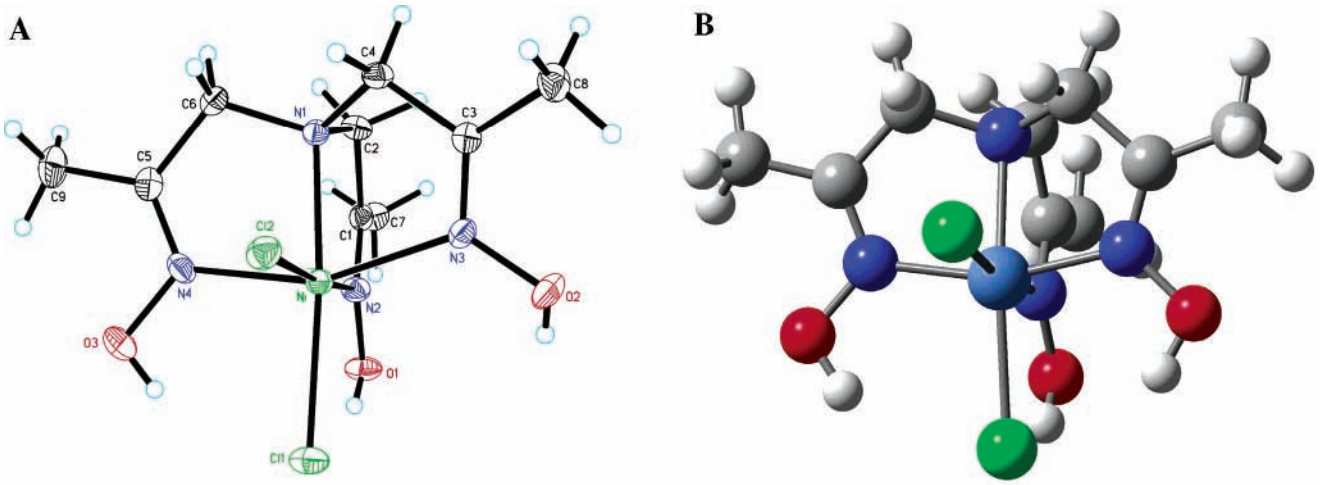

Figure 3. Comparison of molecular geometries from X-ray crystal structure[10] (A) and optimized geometry (B) from method **D** (where C = gray, H = white, Ni = light blue, N = dark blue, O = red, Cl = green). In this X-ray crystal structure, the proton positions were located directly from the difference map and refined; the protons on O3 and O1 are intramolecularly hydrogen bonded to the axial chloride, and the proton on O2 is involved in an intermolecular hydrogen bond.

the theoretical models employed, the intramolecular hydrogen bonding is observed. The main difference between the experimental structure and the theoretical models is that, in the model, all three oxime protons hydrogen bond to the axial chloride. In the crystal structure, intermolecular hydrogen bonding is observed involving the proton of oxime(c) (or O2) and an axial chloride from an adjacent complex. This intermolecular hydrogen bonding lengthens the bonds and significantly alters the angles involving the atoms of oxime(c). This intermolecular interaction also prevents intramolecular hydrogen bonding of this proton to the axial chloride.

The two highest level B3LYP calculations, **C** and **D**, optimize the geometry to the highest possible C_s symmetry, allowing for symmetry of the vibrational modes to be assigned as either A′

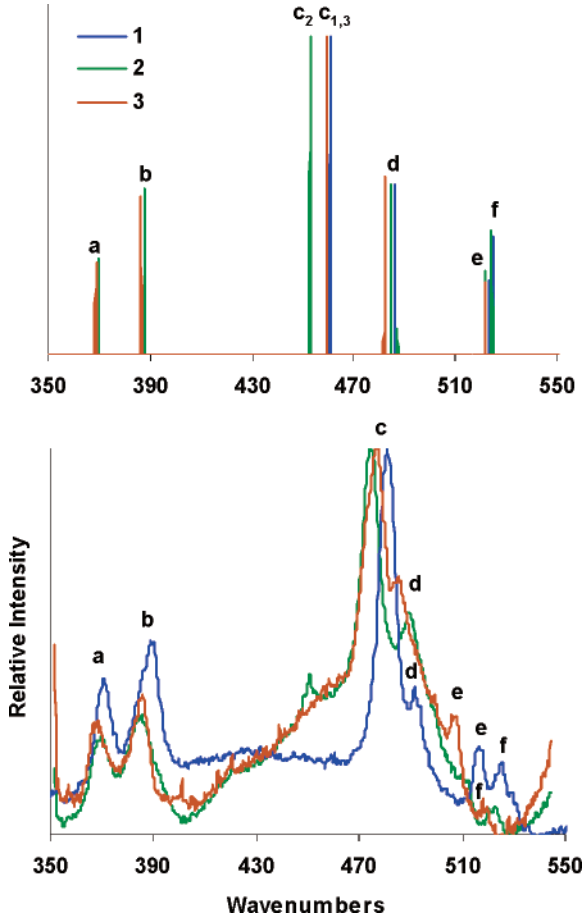

Figure 4. Raman spectra and theoretical frequencies, 350−550 cm^{-1}.

TABLE 3: Raman Spectra and Computational Comparison of the Isotopic Variants of Ni(TRISOXH$_3$)Cl$_2$, 1, 2, and 3

mode[a]	**1 exptl** (calcd)[b]	**2 exptl** (calcd)	**3 exptl** (calcd)
a	**370.7** (369.8)	**370.1** (369.7)	**368.6** (368.5)
b	**389.1** (387.1)	**385.5** (387.1)	**385.9** (386.3)
c	**481.1** (460.5)	**474.2** (452.9)	**477.2** (459.5)
d	**491.5** (486.4)	**487.3** (484.3)	**485.13** (482.1)
e	**516.9** (523.7)	**509.6** (521.9)	**505.9** (516.7)
f	**525.4** (524.7)	**524.0** (524.4)	**519.8** (521.8)
g	**840.5** (849.7)	**839.9** (849.6)	**829.4** (842.5)
h	**848.0** (864.7)	**850.4** (863.6)	**844.2** (857.8)
i	**874.2** (884.6)	**872.0** (883.1)	**865.1** (877.5)
j	**885.5** (894.8)	**891.1** (891.5)	**887.4** (893.9)
w	**1669.4** (1764.4)	**1665.0** (1764.4)	**1646.5** (1741.7)
x	**1693.5** (1766.7)	**1689.4** (1766.5)	**1670.0** (1743.8)
y	**1700.1** (1777.5)	**1702.5** (1777.5)	**1675.6** (1754.5)

[a] For correlation between experimental vibrational frequencies and their assignment and mode descriptions (Table 6), a bold, lower-case letter has been given to each mode. [b] Experimental Raman peaks for **1** and the two ^{15}N-substituted complexes (**2** and **3**) are given in bold and aligned with the calculated value from calculation **C**, given in parentheses.

or A″. All 105 normal modes are both IR and Raman active, however, not all are experimentally observable. This finding is consistent with the calculated intensities for the vibrational frequencies, which imply many modes are too weak to be observed. We focus on those regions of the spectra of principle interest to the chemistry observed for this complex, in particular from approximately 300−1700 cm^{-1}, which describe significant metal−ligand and intraligand vibrations. Many vibrational modes are observable with both Raman and infrared spectroscopic methods, however, for clarity, only the best data for each region of interest are reported. Vibrational modes are assigned

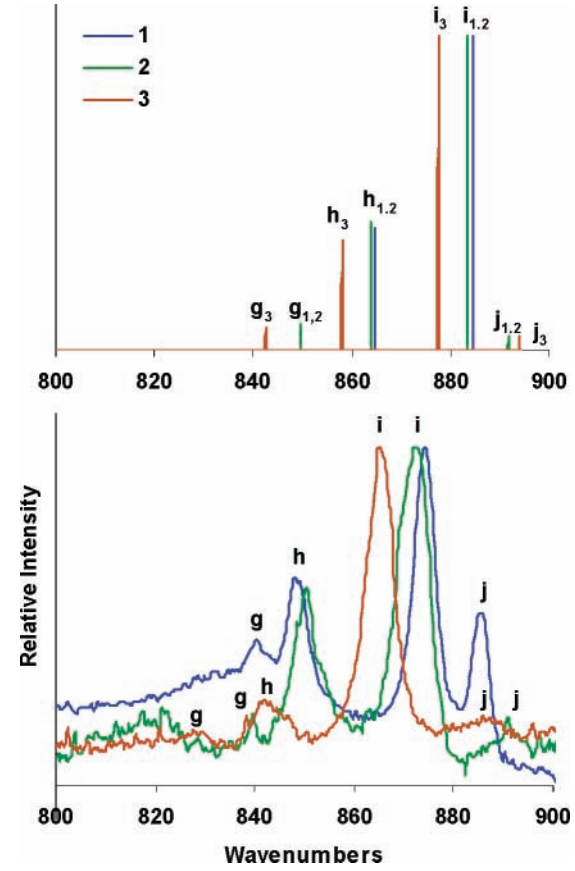

Figure 5. Raman spectra and theoretical frequencies, 800−900 cm^{-1}.

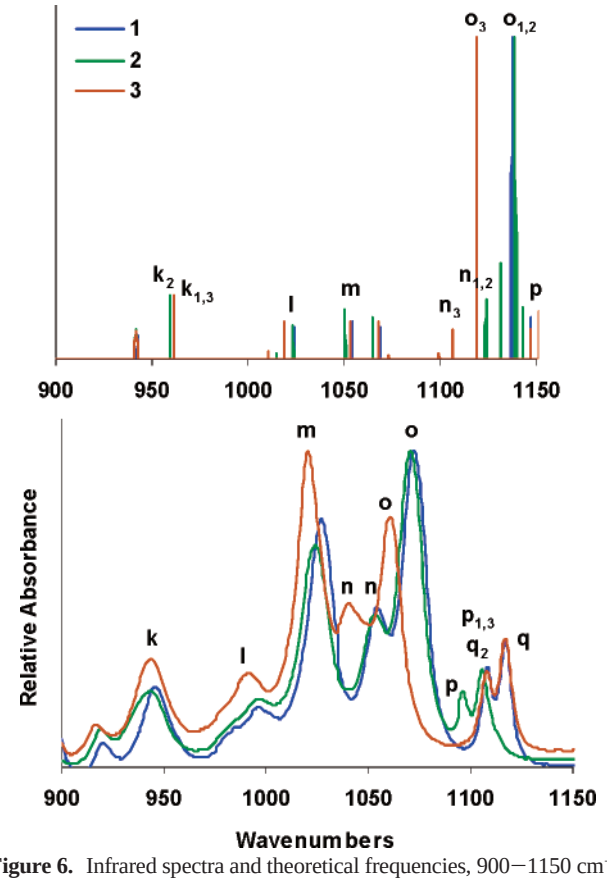

Figure 6. Infrared spectra and theoretical frequencies, 900−1150 cm^{-1}.

a lower-case letter in bold type to aid in the discussion; these data are shown pictorially in Figures 4−8 and tabulated in Tables 3 and 4. These figures contain line spectra which

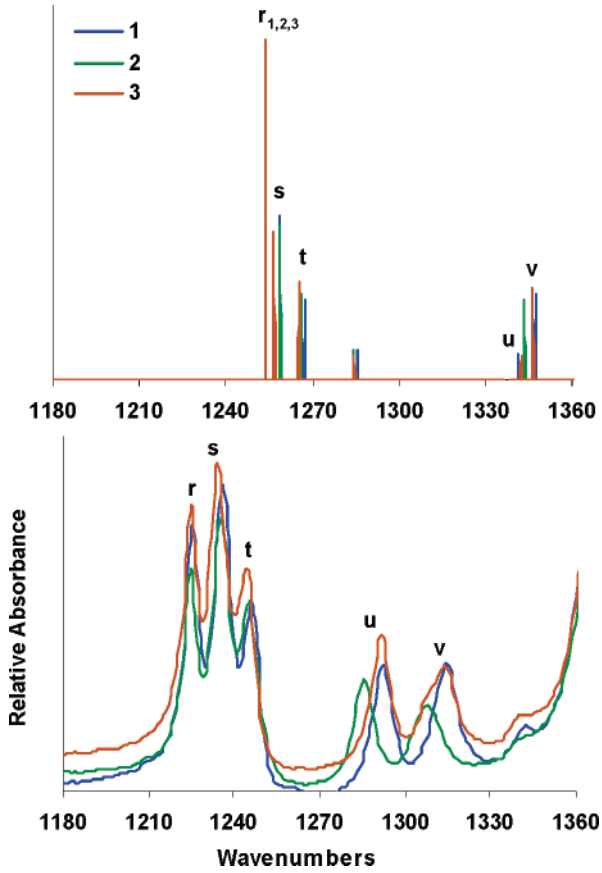

Figure 7. Infrared spectra and theoretical frequencies, 1180−1360 cm^{-1}.

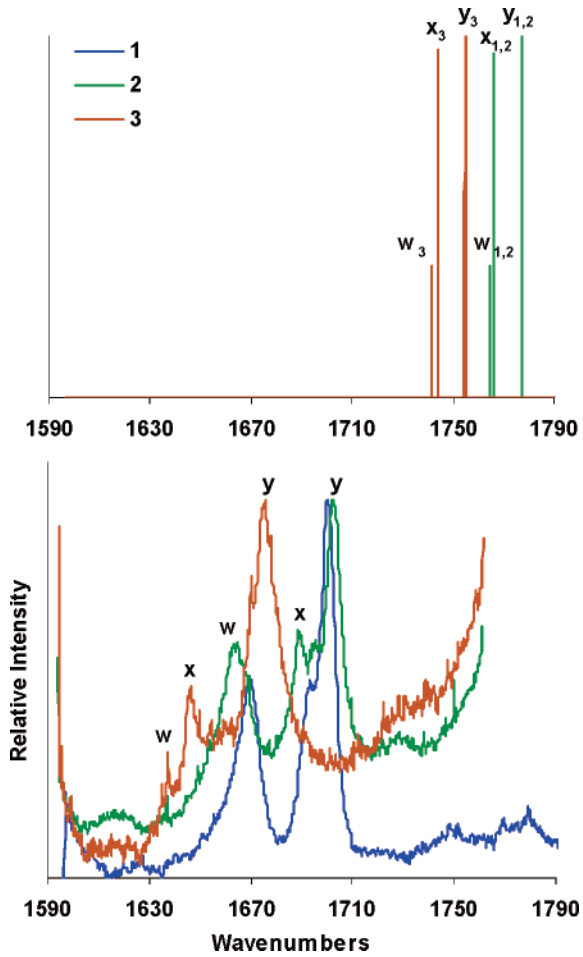

Figure 8. Raman spectra and theoretical frequencies, 1590−1790 cm^{-1}.

correspond to the calculated frequencies and relative intensities; below the line spectra are the corresponding Raman or infrared spectra. Data for the modes involving oxime O−H stretches are reported in Table 5; due to the nature of these vibrational modes, their frequencies are very sensitive to the solid-state environment and thus exhibit much larger deviations from experiment. In order to maximize computational efficiency, reported theoretical data were generated via calculation **C**, the less expensive of the two highest calculations. Subsequent frequency calculations at level **D** yielded minimal differences and no significant improvement in accuracy.

Using isotopically labeled complexes **2**, **3**, and **4**, assignment of 28 observable normal modes was accomplished and is summarized in Table 6. Normal mode assignment was completed by comparing peak position and intensity for observed and theoretical vibrational frequencies. In order to compare observed and theoretical intensities, relative intensities were calculated and used for comparison within each spectral region. Upon isotopic substitution, frequency shifts were observed for those modes involving the substituted atoms; evaluation of the magnitude of these experimental shifts and the corresponding theoretical shifts enabled assignment of the modes. The detailed mode descriptions listed in Table 6 were obtained directly from the calculations.

In the spectral regions shown, there are numerous significant metal−ligand and intraligand modes. Notable is the intense peak observed at 481.1 cm^{-1}, **c** in Figure 4, assigned by noting a shift of 6.9 cm^{-1} upon substitution of ^{15}N for the amine nitrogen. Theoretical calculations predicted a shift of 7.6 cm^{-1} for this substitution, resulting in the assignment of this mode as being dominated by the Ni−N(amine) stretch. Various other modes have metal−ligand character, including primarily intraligand

TABLE 4: Infrared Spectra and Computational Comparison of the Isotopic Variants of Ni(TRISOXH$_3$)Cl$_2$, 1, 2, and 3

mode	**1 exptl** (calcd)	**2 exptl** (calcd)	**3 exptl** (calcd)
k	**948.9** (962.0)	**946.1** (960.1)	**946.1** (961.3)
l	**999.1** (1023.9)	**949.1** (1023.5)	**994.3** (1018.6)
m	**1027.1** (1053.8)	**1021.3** (1049.9)	**1026.1** (1053.4)
n	**1054.1** (1116.4)	**1053.1** (1114.8)	**1042.5** (1099.5)
o	**1072.4** (1137.0)	**1070.5** (1131.2)	**1060.8** (1118.6)
p	**1109.1** (1146.9)	**1096.5** (1138.6)	**1108.1** (1146.6)
q	**1117.7** (1152.5)	**1106.2** (1142.6)	**1117.7** (1151.8)
r	**1225.8** (1253.9)	**1224.8** (1253.8)	**1224.8** (1253.6)
s	**1236.4** (1258.8)	**1235.4** (1258.7)	**1234.4** (1257.1)
t	**1246.0** (1267.0)	**1245.0** (1266.3)	**1244.1** (1265.2)
u	**1292.3** (1343.3)	**1285.6** (1337.1)	**1291.3** (1343.1)
v	**1314.5** (1347.6)	**1307.7** (1343.8)	**1313.5** (1346.8)

TABLE 5: Infrared Spectra and Computational Comparison of the Isotopic Variants of Ni(TRISOXH$_3$)Cl$_2$, 1, and 4

mode	**1 exptl** (calcd)	**4 exptl** (calcd)
z	**3162.3** (3304.2)	**2364.7** (2408.1)
aa	**3243.3** (3566.0)	**2442.8** (2598.9)
bb	**3333.9** (3579.4)	**2465.0** (2608.3)

modes **g**, **h**, **i**, and **j** in Figure 5. Assignment of these four modes reveals that each is mainly a breathing mode of a combination of ligand arms, but the modes also exhibit significant Ni−N(oxime) stretching. For the three peaks observed between 1590 and 1790 cm^{-1}, **w**, **x**, and **y** in Figure 8, experimental data for **2** show no isotope shifting and **3** clearly shows a large shift of at least 23 cm^{-1}, demonstrating that these modes involve the oxime nitrogens. Theoretical calculations predict no shift of the

TABLE 6: Vibrational Mode Assignment of Ni(TRISOXH$_3$)Cl$_2$

mode	experiment [a]	assigned wavenumber unscaled[b]	assigned wavenumber scaled[c]		symmetry[d] and mode description[e]
a	370.7	369.8	394.6	A′	TRISOXH$_3$ breathing mode, arm b out-of-phase (OOP) with arms a, c
b	389.1	387.1	410.5	A″	OOP ∠CH$_2$(a)−N1−CH$_2$(b) and ∠CH$_2$(b)−N1−CH$_2$(c) bend
c	481.1	460.5	477.9	A′	Ni−N1 stretch
d	491.5	486.4	501.7	A′	∠N(a)−Ni−Cl(eq) and ∠N(c)−Ni−Cl(eq) bend
e	516.9	523.7	536.0	A′	oxime H(a) and oxime H(c) wagging
f	525.4	524.7	536.9	A″	OOP oxime H(a) and oxime H(c) wagging, arm b torsion
g	840.5	849.7	835.5	A″	OOP breathing mode of arms a, c with some Ni−N(a,c) stretch
h	848.0	864.7	849.2	A′	breathing mode of arm b with some Ni−N(b) stretch
i	874.2	884.6	867.5	A′	breathing mode of arms a,b,c with some Ni−N(a,b,c) stretch
j	885.5	894.8	876.9	A′	N1−CH$_2$(a,b,c) stretch, some OOP Ni−N1 and Ni−N(b) stretch
k	948.9	962.0	938.6	A′	CH$_2$ and CH$_3$ (a,c) rock
l	999.1	1023.9	995.5	A′	CH$_3$(b) rock, some Ni−N(b) stretch
m	1027.1	1053.8	1022.9	A″	CH$_3$(a,b,c) rock, some N1−CH$_2$(a,b,c) stretch
n	1054.1	1116.4	1080.4	A″	N−O(a,c) stretch
o	1072.4	1137.0	1099.4	A′	N−O(a,b,c) stretch
p	1109.1	1146.9	1108.5	A′	OOP N1−CH$_2$(b) and N1−CH$_2$(a,c) stretch
q	1117.7	1152.5	1113.6	A″	OOP N1−CH$_2$(a,c) and N1−CH$_2$(b) stretch
r	1225.8	1253.9	1206.7	A″	CH$_2$(a,c) twist, OOP ∠C═N−O(a) and ∠C═N−O(c) bend
s	1236.4	1258.8	1211.2	A′	H$_2$C−C(b) stretch, ∠H(a,c)−O−N compression, ∠H(b)−O−N expansion
t	1246.0	1267.0	1218.8	A′	H$_2$C−C(a,c) stretch, ∠H(a,b,c)−O−N expansion
u	1292.3	1343.3	1288.9	A″	CH$_2$(a,b,c) twist, OOP N1−CH$_2$(a) and N1−CH$_2$(c) stretch
v	1314.5	1347.6	1292.8	A′	OOP CH$_2$(a,c) twist and N1−CH$_2$(b) stretch
w	1669.4	1764.4	1675.7	A″	OOP C═N(a) and C═N(c) stretch
x	1693.5	1766.7	1677.8	A′	C═N(a,c) stretch, small C═N(b) stretch
y	1700.1	1777.5	1687.7	A′	C═N(b) stretch, small C═N(a,c) stretch
z	3162.3	3304.2	3090.1	A′	O−H(b) stretch
aa	3243.3	3566.0	3330.6	A″	OOP O−H(a) and O−H(c) stretch
bb	3333.9	3579.4	3342.9	A′	O−H(a,c) stretch

[a] Natural abundance wavenumber data reported from both Raman and infrared experiments; see Tables 4 and 5 for further information. [b] Theoretical data assigned from calculation **C** (ub3lyp/6-31G(d)&6-311+G(d)); further accuracy was not observed for the frequencies generated from calculation **D**. [c] Assigned theoretical vibrational frequencies (cm^{-1}) were scaled by applying eq 1. [d] The optimized geometry for Ni(TRISOXH$_3$)Cl$_2$ has C_s symmetry which places a mirror in the plane of arm b of the ligand and through each halide; mode symmetry was theoretically determined. [e] Letter designations for atoms are the same as in Table 2, utilizing a, b, and c to represent the three arms of the TRISOXH$_3$ ligand and atoms therein. "Breathing modes" for arms a, b, and c involve all atoms. "Twist" and "rock" modes involve two or more atoms moving together, while "wag" modes are dominated by one atom motion. OOP indicates the modes are out-of-phase with respect to each other, and are not necessarily antisymmetric with respect to the mirror plane.

modes in this region for **2** and shifts of 22−23 cm^{-1} for **3**, enabling the assignment of these experimentally observed modes as C═N stretches.

The calculated frequencies over 630 cm^{-1} are consistently overestimated and the difference between theoretical and observed values grows increasingly large as the energies of the modes increase. The hybrid functional B3LYP employed here has been shown to produce the most correct vibrational frequencies.[24] Moreover, improving the wave function by adding in electron correlation and increasing the basis set diminishes the need for empirical correction.[25] However, to date, there is no standardized method of scaling frequencies generated from DFT calculations using split basis sets. Various approaches to scaling calculated vibrational frequencies have been employed for simple molecules; the simplest is a uniform scale factor, usually a value less than 1 for B3LYP calculations.[26] Zhang et al. applied an empirically determined uniform factor of 1.12 to palladium and platinum halide complexes optimized by the Hartree−Fock method.[27] In several recent publications, a modified scaled quantum mechanical force field procedure was applied to a training set of organic and simple inorganic complexes to correct for anharmonicity. Standard scale factors are available for the organic portions of the complex, but must be derived for any metal−ligand interactions, and there is no consideration for split basis set calculations.[25,28] A third type of scaling uses wavenumber−linear scale (WLS) factors where a linear fit is made between the scale factor and vibrational wavenumber. Yoshida et al. correlated experimentally assigned vibrational modes with hybrid DFT calculated frequencies for more than 350 organic and inorganic compounds and concluded that the WLS method is a good correction for anharmonicity.[24,29] In this work, we made vibrational assignments empirically via isotopic shifts and, because of the large size of the Ni complex and the split basis set calculation employed, we employed a modified version of the wavenumber−linear scaling method. After assigning the principle observed vibrational modes, each was directly compared with its theoretical counterpart; the resulting graph is shown in Figure 9. A linear fit was applied (R^2 = 0.9989), and the resulting equation (eq 1) was used to scale the calculated frequencies, summarized in Table 6.

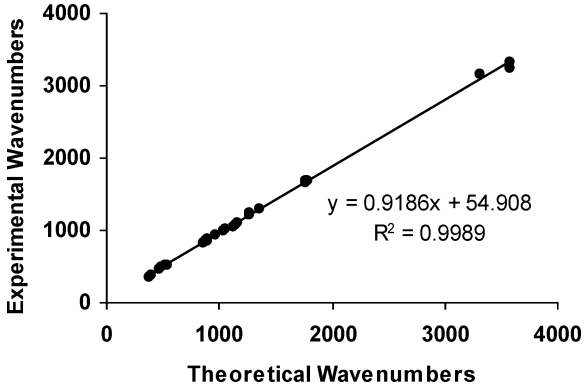

Figure 9. Linear correlation between experimental and assigned theoretical wavenumbers.

$$\nu_{\text{scaled}} = 0.9186\nu_{\text{unscaled}} + 54.908\ \text{cm}^{-1} \qquad (1)$$

Discussion

This work details the development and calibration of a theoretical model for an interesting nickel complex, $Ni(TRISOXH_3)Cl_2$. The use of density-functional theory for transition metal complexes has precedence and has been utilized here with success. Significant improvement in modeling the geometry of the complex is shown when moving from Hartree−Fock to the hybrid functional B3LYP and larger split basis sets. The best optimized geometry obtained from calculation **D** results in only a 1.0% average deviation from the experimental bond lengths.

With regard to the frequency calculations, there are very minimal differences between frequencies generated by **C** and **D**. Expense considerations become significant at these levels of calculations; the accuracy obtained by going to a higher basis set must be weighed with the computational cost. Although **D** gave the best optimized geometry results, it was more expensive than **C** and did not show significant improvement in modeling the vibrational modes. This observation, consistent with the findings of Bytheway et al.,[30] suggests basis set choice is less critical for calculating vibrational modes than for modeling molecular geometries. For future calculations on similar nickel complexes, level **C** will be primarily used, notably in the calculation of vibrational frequencies for putative intermediates.

Although the calculated vibrational frequencies significantly deviate from experiment, the correlation is very linear. The application of a linear scaling function significantly improves the accuracy of the theoretical vibrational wavenumbers. An average percent deviation of 3.1% (from 0.7 to 322.7 cm^{-1}, averaging 52 cm^{-1}) for the unscaled valued is reduced to 1.6% (from 0.6 to 87.3 cm^{-1}, averaging 17.4 cm^{-1}) by applying the derived linear scale function: a 2-fold improvement over the unscaled percent deviations (3-fold in wavenumbers). This error minimization is similar and at least as satisfactory as the improvements reported by Yoshida et al.[24] Evaluation of the deviations for individual vibrational modes before and after scaling enabled significant outliers to be identified and, in one case, resulted in correction of a previously ambiguous assignment.

As expected, the intermolecular hydrogen bonding observed in the crystal structure is not reproduced in the gas-phase single complex computational model. Nonetheless, the DFT calculations do successfully model bond lengths and intramolecular hydrogen bonding with minimal errors. Theoretical intensities for the vibrational modes were difficult to utilize alone, though the relative intensities provided a guide for vibrational mode assignment. The use of isotope-substituted complexes, in conjunction with this theoretical model, facilitated the assignment of the key vibrational modes. Effectively, this work serves as a calibration of confidence in high-level DFT models for application to $Ni(TRISOXH_3)Cl_2$ and related compounds. The developed and calibrated model can now be applied to less well-characterized species and facilitate our understanding of the experimentally inaccessible intermediates in the complex's reaction with oxygen. The vibrational mode assignments will serve as a reference for studies now in progress, which will lead to insight into the mechanistic details of the deprotonated complex's reaction with molecular oxygen.

This work demonstrates the effective DFT computational modeling of the geometry and vibrational frequencies of a large paramagnetic transition metal complex. As expected, addition of polarization and diffuse functions to the metal center basis set is shown to increase accuracy, notably in reproducing the metal−ligand bond lengths. If accurate molecular geometries are the goal of the computational model, the improvements gained with increasingly expensive calculations are significant. However, the increasing expense of using higher level basis sets does not necessarily result in improved predictions of vibrational frequencies. Significant deviations from experimental vibrational frequencies are minimized by exploiting the linear correlation between theoretical and experimental vibrational modes. By serving as a correction for anharmonicity, the empirically determined linear scale function successfully minimizes deviations from experiment and aids in ambiguous mode assignment. In future investigations of related complexes, unique linear scale functions can be derived by following the method established in this study of $Ni(TRISOXH_3)Cl_2$.

Acknowledgment. The authors thank Professor Thomas Beck and Dr. Anping Liu of the University of Cincinnati for helpful discussions and facilitating the molecular-modeling experiments. We also thank Professor Richard Hotz (College of Mount St. Joseph, Cincinnati, Ohio) for synthesis of the ^{15}N isotope-labeled ligands. Acknowledgment is made to the donors of the Petroleum Research Fund administered by the American Chemical Society (ACS-PRF 37653-AC3) who funded this research. Funding was also provided by the Department of Chemistry, University of Cincinnati.

Supporting Information Available: Table 1S, results from calculations **E**−**G**; Table 2S, complete list of 105 vibrational modes calculated with level **C**; Figure 1S, infrared spectra and theoretical frequencies for **1** and **4**, 1900−3800 cm^{-1}. This material is available free of charge via the Internet at http://pubs.acs.org.

References and Notes

(1) Koch, W.; Holhausen, M. C. *A Chemist's Guide to Density Functional Theory*; Wiley-VCH: Weinheim, 2000.

(2) Ziegler, T. *Chem. Rev.* **1991**, *91*, 651.

(3) Ziegler, T. *Can. J. Chem* **1995**, *73*, 743.

(4) Neese, F.; Solomon, E. I. *J. Am. Chem. Soc.* **1998**, *120*, 12829.

(5) Chen, P.; Fujisawa, K.; Solomon, E. I. *J. Am. Chem. Soc.* **2000**, *122*, 10177.

(6) Szilagyi, R. K.; Metz, M.; Solomon, E. I. *J. Phys. Chem. A* **2002**, *106*, 2994.

(7) Wheeler, D. E.; Rodriguez, J. H.; McCusker, J. K. *J. Phys. Chem.* **1999**, *103*, 4101.

(8) Li, S.; Hall, M. B. *Inorg. Chem.* **2001**, *40*, 18.

(9) Goldcamp, M. J.; Robison, S. E.; Krause-Bauer, J. A.; Baldwin, M. J. *Inorg. Chem.* **2002**, *41*, 2307.

(10) Goldcamp, M. J.; Edison, S. E.; Squires, L. N.; Rosa, D. T.; Vowels, N. K.; Coker, N. L.; Krause-Bauer, J. A.; Baldwin, M. J. *Inorg. Chem.* **2003**, *42*, 717.

(11) Sheldon, R. A. Biocatalytic and Biomimetic Oxidations from an Industrial Perspective. In *Biomimetic Oxidations Catalyzed by Transition Metal Complexes*; Meunier, B., Ed.; Imperial College Press: London, 2000; p 613.

(12) Sheldon, R. A.; Kochi, J. K. *Metal-Catalyzed Oxidations of Organic Compounds*; Academic Press: New York, 1981.

(13) Sproul, G.; Stucky, G. D. *Inorg. Chem.* **1973**, *12*, 2898.

(14) Singh, A. N.; Singh, R. P.; Mohanty, J. G.; Chakravorty, A. *Inorg. Chem.* **1977**, *16*, 2597.

(15) Mohanty, J. G.; Singh, R. P.; Chakravorty, A. *Inorg. Chem.* **1975**, *14*, 2178.

(16) Martone, D. P.; Osvath, P.; Lappin, A. G. *Inorg. Chem.* **1987**, *26*, 3094.

(17) Korvenranta, J.; Saarinen, H.; Nasakkala, M. *Inorg. Chem.* **1982**, *21*, 4296.

(18) Matthaiopoulos. *Chem. Ber.* **1898**, *31*, 2396.

(19) Ogloblin, K. A.; Potekhin, A. A. *J. Org. Chem. USSR (Engl. Transl.)* **1965**, *1*, 399.

(20) Frisch, M. J.; Trucks, G. W.; Schlegel, H. B.; Scuseria, G. E.; Robb, M. A.; Cheeseman, J. R.; Zakrzewski, V. G.; Montgomery, J. A., Jr.; Stratmann, R. E.; Burant, J. C.; Dapprich, S.; Millam, J. M.; Daniels, A.

D.; Kudin, K. N.; Strain, M. C.; Farkas, O.; Tomasi, J.; Barone, V.; Cossi, M.; Cammi, R.; Mennucci, B.; Pomelli, C.; Adamo, C.; Clifford, S.; Ochterski, J.; Petersson, G. A.; Ayala, P. Y.; Cui, Q.; Morokuma, K.; Malick, D. K.; Rabuck, A. D.; Raghavachari, K.; Foresman, J. B.; Cioslowski, J.; Ortiz, J. V.; Stefanov, B. B.; Liu, G.; Liashenko, A.; Piskorz, P.; Komaromi, I.; Gomperts, R.; Martin, R. L.; Fox, D. J.; Keith, T.; Al-Laham, M. A.; Peng, C. Y.; Nanayakkara, A.; Gonzalez, C.; Challacombe, M.; Gill, P. M. W.; Johnson, B. G.; Chen, W.; Wong, M. W.; Andres, J. L.; Head-Gordon, M.; Replogle, E. S.; Pople, J. A. *Gaussian 98*, revision A.11; Gaussian, Inc.: Pittsburgh, PA, 1998.

(21) Becke, A. D. *J. Chem. Phys.* **1993**, *98*, 5648.

(22) Lee, C.; Yang, W.; Parr, R. G. *Phys. Rev. B* **1988**, *37*, 785.

(23) Perdew, J. P. *Phys. Rev. B* **1986**, *B 33*, 882.

(24) Yoshida, H.; Takeda, K.; Okamur, J.; Ehara, A.; Matsuura. *J. Phys. Chem. A* **2002**, *106*, 3580.

(25) Baker, J.; Jarzecki, A. A.; Pulay, P. *J. Phys. Chem. A* **1998**, *102*, 1412.

(26) Foresman, J. B.; Frisch, A. *Exploring Chemistry with Electronic Structure Methods*, 2nd ed.; Gaussian, Inc.: Pittsburgh, PA, 1996.

(27) Zhang, L.; Wei, H.; Zhang, Y.; Guo, Z.; Zhu, L. *J. Phys. Chem. A* **2002**, *106*, 3819.

(28) Diaz-Acosta, I.; Baker, J.; Cordes, W.; Pulay, P. *J. Phys. Chem. A* **2001**, *105*, 238.

(29) Yoshida, H.; Ehara, A.; Matsuura, H. *Chem. Phys. Lett.* **2000**, *325*, 477.

(30) Bytheway, I.; Wong, M. W. *Chem. Phys. Lett.* **1998**, *282*, 219.